CHEMISTRY OF MATERIALS

Article

pubs.acs.org/cm

Structural, Magnetic, and Electrical Properties of $Bi_{1-x}La_xMnO_3$ (x = 0.0, 0.1, and 0.2) Solid Solutions

Wei-Tin Chen,[†] Falak Sher,[‡] Neil D. Mathur,[§] Christopher M. Kavanagh,[∥] Finlay D. Morrison,[∥] and J. Paul Attfield*,[†]

[†]Centre for Science at Extreme Conditions and School of Chemistry, University of Edinburgh, Mayfield Road, Edinburgh EH9 3JZ, United Kingdom

[‡]Department of Chemistry, School of Science and Engineering, Lahore University of Management Sciences (LUMS), Lahore, Pakistan

[§]Department of Materials Science, University of Cambridge, Pembroke Street, Cambridge CB2 3QZ, United Kingdom

[∥]EaStCHEM School of Chemistry, University of St Andrews, St Andrews KY16 9ST, United Kingdom

ABSTRACT: Possible ferromagnetic and ferroelectric orders in ceramic $Bi_{1-x}La_xMnO_3$ (x = 0.0, 0.1, and 0.2) samples prepared under 3−6 GPa pressure have been investigated. Rietveld fits to powder neutron diffraction data show that $BiMnO_3$ and $Bi_{0.9}La_{0.1}MnO_3$ adopt a monoclinic $C2/c$ perovskite superstructure whereas $Bi_{0.8}La_{0.2}MnO_3$ has orthorhombic $Pnma$ symmetry. Both structural analysis and Curie−Weiss fits to magnetic susceptibility data show that high spin d^4 Mn^{3+} is present with no significant Bi deficiency or Mn^{4+} content apparent. La substitution suppresses the magnetic Curie temperature of the monoclinic phase from 105 K for x = 0 to 94 K at x = 0.1, but the x = 0.2 material shows antiferromagnetic order similar to that of $LaMnO_3$. Impedance spectroscopy and dielectric measurements on the x = 0.1 and 0.2 materials show modest bulk permittivity values (45−80) down to 50 K, and there is no strong evidence for ferroelectric behavior. The two samples have thermally activated conductivities with activation energies of 0.21−0.24 eV.

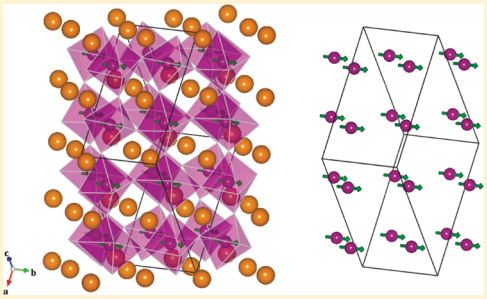

KEYWORDS: *high pressure synthesis, multiferroic, Perovskite, magnetism, ferroelectricity, manganites*

1. INTRODUCTION

Multiferroic materials show the coexistence of at least two orders such as (anti)ferroelectricity, (anti)ferromagnetism, and ferroelasticity.[1−6] The multifunctional character of these materials and the possibility of manipulating one order parameter through the other leads to potential applications in information storage, magnetic tunnel junctions, and logic gates.[7,8] A single multiferroic phase with strong coupling between ferroelectric and ferromagnetic order parameters may enable magnetic polarization to be controlled with an applied electric field. Only a small number of materials exhibit practical multiferroic properties, and these usually show a very weak coupling between the ferroelectric and the ferromagnetic order parameters. The perovskite $BiFeO_3$ is one of the most widely studied multiferroic materials because it can be synthesized at ambient pressure, and the ferroelectric Curie temperature, T_E = 1100 K, and antiferromagnetic Neel temperature, T_N = 640 K, are both well above room temperature.[9−11] A number of manganese-based perovskite oxides such as $BiMnO_3$,[6] $YMnO_3$,[12] $TbMnO_3$,[13] $TbMn_2O_5$,[14] and so forth are also reported to show multiferroic properties.

$BiMnO_3$ and derived solid solutions are less studied than $BiFeO_3$ analogues because synthesis of bulk $BiMnO_3$ requires high pressure. However, thin films of $BiMnO_3$ materials can be prepared at ambient pressure through epitaxial stabilization by the substrate.[15] $BiMnO_3$ is a ferromagnetic insulator with Curie temperature $T_C \approx 100$ K[16] and a saturation magnetization of 3.9 μ_B/Mn.[17] There are also claims of ferroelectric behavior below a ferroelectric Curie temperature, T_E, of 450 K.[18,19] $BiMnO_3$ was reported to have an acentric, monoclinic, perovskite superstructure with $C2$ space group.[20] However, density functional calculations predicted a centrosymmetric structure with space group $C2/c$.[21] Belik et al.[22] reported refined structures with $C2/c$ symmetry in both the low and the high temperature regimes. An orthorhombic phase (space group $Pnma$) has been reported from above 768 K to the decomposition temperature.[23] The structure of $BiMnO_3$ can also be transformed to an orthorhombic phase (space group $Pnma$) above 8 GPa pressure,[24,25] which is reported to have an orbital order similar to that of $LaMnO_3$ but with a different arrangement in the ac plane. Several oxygen-rich $BiMnO_{3+\delta}$ structures have also been reported.[6,26]

The difference between ferromagnetic $BiMnO_3$ and A-type antiferromagnetic $LaMnO_3$[27] is striking in view of the similar ionic radii[28] of La^{3+} and Bi^{3+} and is attributed to polar distortions originating from Bi^{3+} $6s^2$ lone pairs.[29,30] Hence, solid solutions

Received: September 27, 2011
Revised: November 24, 2011
Published: November 29, 2011

between the two phases are of interest. Troyanchuk et al.[31] showed that bulk, homogeneous $Bi_{1-x}La_xMnO_3$ solid solutions with $0.35 \leq x \leq 1$ are accessible at ambient pressure, but high pressure synthesis is needed for lower x. A change from orthorhombic to monoclinic symmetry and an increase in magnetization on decreasing from $x = 0.2$ to $x = 0.1$ were noted, but structural information and magnetic data were not reported. Gajek et al.[8,15] reported that epitaxial thin films of $Bi_{0.9}La_{0.1}MnO_3$ are ferromagnetic and ferroelectric and retain both orders down to a thickness of 2 nm. They suggested that Bi site deficiency and the resulting introduction of Mn^{4+} (d^3) ions was responsible for the ferromagnetic properties, whereas ferroelectricity was linked to the directional nature of $6s^2$ lone pair of Bi^{3+} ions. To clarify the structural and possible multiferroic properties of Bi-rich $Bi_{1-x}La_xMnO_3$ materials, we report here high pressure syntheses, crystal structures determined from neutron powder diffraction data, and magnetic and detailed electrical property measurements of bulk $Bi_{1-x}La_xMnO_3$ (x = 0.0, 0.1, and 0.2) samples.

2. EXPERIMENTAL SECTION

2.1. Synthesis. A multianvil Walker press method previously employed to prepare other high pressure perovskites[32−34] was used for high pressure synthesis of $Bi_{1-x}La_xMnO_3$ (x = 0.0, 0.1, and 0.2) samples. Stoichiometric amounts of 99.99% pure Bi_2O_3, La_2O_3, and Mn_2O_3 (all from Aldrich) were weighed, mixed, and ground well in a mortar and pestle. The ground starting materials were sealed in a gold capsule and placed in a boron nitride (BN) container and pressure cell assembly. The gold capsule was found to be essential to avoid reaction of the starting materials with the BN container during sintering. Pressure was applied hydrostatically by a uniaxial force through steel wedges and tungsten carbide (WC) anvils to the assembled cell by a Walker type press. Pressure was increased at 3 GPa·h^{-1} up to the synthesis pressures shown in Table 1. Different combinations of pressure, sintering temperatures, and heating durations were tried to minimize the proportion of impurity phases in the final products. It was found that at least 60 min of heating was required for complete reaction, after which samples were quenched. The optimum synthesis conditions for three samples are listed in Table 1. Each synthesis produced a bulk, dark gray cylindrical ceramic product of mass ∼ 20 mg. Some samples were ground to a black powder and combined for magnetic and diffraction measurements, whereas as-prepared materials were used for the electrical measurements.

Table 1. Synthesis Conditions and Magnetic Parameters for $Bi_{1-x}La_xMnO_3$ Materials ($0 \leq x \leq 0.2$)[a]

sample	x = 0.0	x = 0.1	x = 0.2
pressure (GPa)	6.0	4.5	3.0
temperature (°C)	1100	900	800
T_C (K)	101	94	80
θ (K)	114	110	41
C (cm^3·K·mol^{-1})	3.53	3.12	3.28
μ_{eff} (μ_B/Mn^{3+})	5.32	5.00	5.13
M_s (μ_B/Mn^{3+})	3.67	3.17	0.97
M_r (μ_B/Mn^{3+})	0.07	0.26	0.24
H_c (Oe)	30	120	350

[a]Samples were heated up to the indicated temperature in 10 min and quenched after a heating period of 60 min. Curie temperatures and Curie-Weiss fit parameters (Weiss temperature, Curie constant, and paramagnetic moment) are from susceptibility measurements in an applied field of 100 Oe. Saturated and remnant magnetizations and the coercive field are from hysteresis loops measured at 5 K.

2.2. X-ray and Neutron Powder Diffraction. Samples were characterized by a Bruker D8 Advance X-ray diffractometer using flat plate mode. X-ray diffraction (XRD) patterns were collected in the range of $5° \leq 2\theta \leq 98°$ with an integration time of 5 s per 0.01355° step with Ge(111) monochromator and Cu $K\alpha_1$ radiation (λ = 1.540598 Å) at ambient conditions. Time-of-flight (TOF) neutron powder diffraction (NPD) data from the three compositions were collected at 20 and 150 K on the general materials diffractometer (GEM) at the ISIS pulsed neutron source facility, Rutherford Appleton Laboratory, UK. Samples (∼100 mg) were loaded in a 3.0 mm diameter vanadium can, and diffraction data at each temperature were collected from six detector banks for ∼5 h. The XRD and NPD patterns were analyzed by the Rietveld refinement method using the General Structure Analysis System (GSAS) program.[35]

2.3. Magnetic Properties. Magnetic properties of the samples were measured with a Quantum Design MPMS XL SQUID magnetometer. Temperature-dependent DC susceptibility was collected in the temperature range of 5−300 K in zero-field-cooled (ZFC) and a field-cooled (FC) modes with an applied field of 100 Oe. Magnetization-field hysteresis loops were recorded at a temperature of 5 K under magnetic fields varying from −70 to +70 kOe.

2.4. Electrical Characterization. Impedance spectroscopy measurements were carried out in the frequency range 5 Hz−10 MHz using a combination of HP4192A and Agilent 4294A impedance analyzers and in the temperature range 340−50 K using a closed cycle He-cryocooler. Impedance spectra were obtained isothermally at ca. 25 K intervals; fixed frequency capacitance (C_p) and loss (D) data were also collected under fixed rate cooling/heating at 2 K min^{-1}. Electrodes were fabricated on opposing sample faces by sputtered Au through a shadow mask, and all data were corrected for sample geometry [(electrode area, A (cm^2), and sample thickness, d (cm)] prior to analysis using the ZView software suite.[36] In all cases the ac excitation voltage was 100 mV, with overlying dc bias up to a maximum of ±35 V (corresponding to maximum fields of ca. 850 V cm^{-1}).

3. RESULTS

3.1. Crystal Structures. $Bi_{1-x}La_xMnO_3$ (x = 0.0, 0.1, and 0.2) samples were initially analyzed using laboratory X-ray diffraction. A monoclinic structure model in space group $C2/c$ (No. 15) with atomic positions Bi, 8f (x, y, z); Mn1, 4e (0, y, 3/4); Mn2, 4d (1/4, 1/4, 1/2); O, 8f (x, y, z) from the work of Montanari et al.[37] was adopted for XRD data analysis of the $BiMnO_3$ sample. Rietveld refinement yielded the following lattice parameters: a = 9.5384(3) Å, b = 5.6103(2) Å, c = 9.8565(3) Å, and β = 110.639(1)°. A minor impurity phase of α-Bi_2O_3 was also observed and was included in the final refinements. Neutron diffraction data collected at 20 and 150 K for $BiMnO_3$ did not reveal the presence of any new nuclear scattering peaks, and so the room temperature monoclinic model was used to Rietveld-fit the data. Multi-histogram refinements were carried out using GEM data collected from detector banks 1−5. Fitted $BiMnO_3$ profiles from selected data banks and the XRD data are shown in Figure 1. Refined lattice parameters, atom positions, and resulting selected bond distances are listed in Table 2. Refinement of site occupancies confirmed that all sites are fully occupied. No lattice anomaly is evident between 20 and 300 K. The Jahn−Teller distortion of the oxide octahedron around the Mn^{3+} cation is evident from the Mn−O bond distances.

Comparison of XRD patterns for $BiMnO_3$ and $Bi_{0.9}La_{0.1}MnO_3$ showed that both materials adopt the same crystal structure. Thus, the $C2/c$ model from the $BiMnO_3$ refinements was used to fit the $Bi_{0.9}La_{0.1}MnO_3$ XRD and NPD data. However, a small amount of orthorhombic *Pnma* symmetry $Bi_{1-x}La_xMnO_3$ perovskite (weight fraction 5.0(2)%) was also observed. It was not possible to refine the Bi/La content of this phase independently, so it was constrained to have the same x = 0.1 composition as the main monoclinic phase. Two other impurity phases, Mn_3O_4 and α-Bi_2O_3, were also present, and

dx.doi.org/10.1021/cm202900v | Chem. Mater. 2012, 24, 199−208

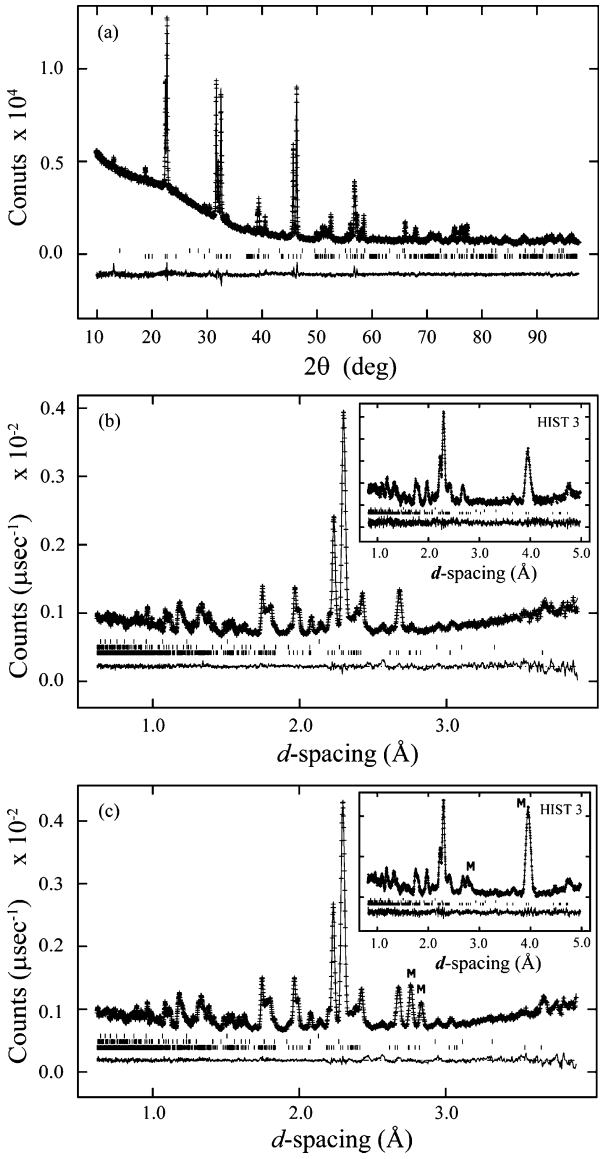

Figure 1. Rietveld fits of $BiMnO_3$ for (a) D8 XRD pattern at room temperature, (b) GEM NPD pattern from bank 4 and bank 3 (inset) at 150 K, and (c) GEM NPD pattern from bank 4 and bank 3 (inset) at 20 K, while the magnetic reflections are marked by "M". The index markers from the bottom represent the reflections of $BiMnO_3$ (99(7) %), α-Bi_2O_3 (1(7) %), and V container (GEM data only), respectively.

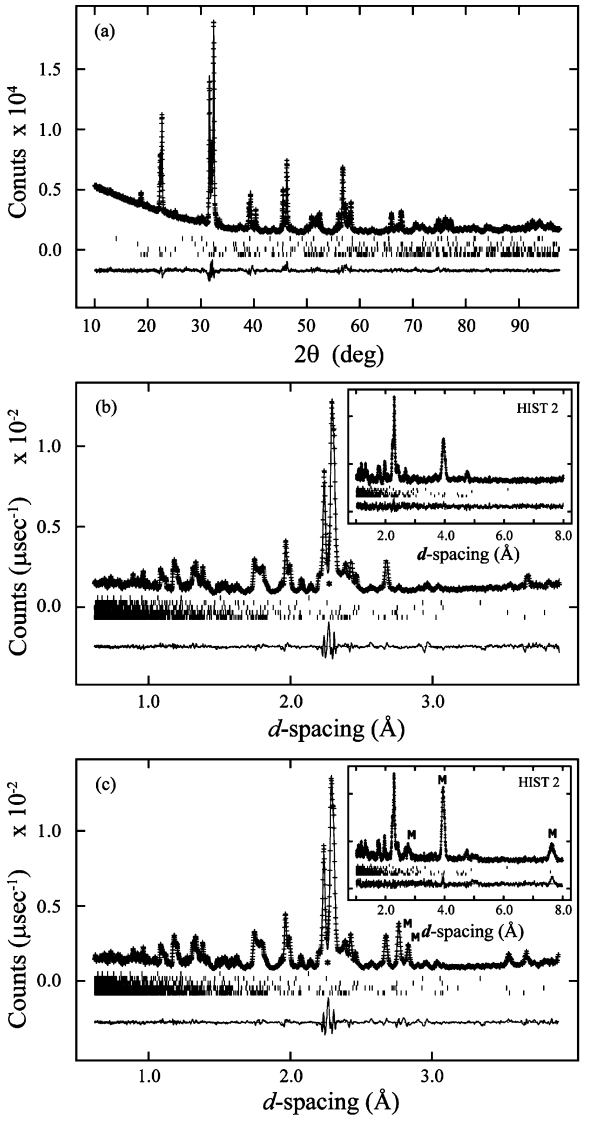

Figure 2. Rietveld fits of $Bi_{0.9}La_{0.1}MnO_3$ for (a) D8 XRD pattern at room temperature, (b) GEM NPD pattern from bank 4 and 2 (inset) at 150 K, and (c) GEM NPD pattern from bank 4 and 2 (inset) at 20 K; the magnetic reflections are marked by "M". The index markers from the bottom represent the reflections of $Bi_{0.9}La_{0.1}MnO_3$ (90(2) %), Bi/$LaMnO_3$ orthorhombic phase (5.0(2) %), Mn_3O_4 (1.1(1) %), α-Bi_2O_3 (4.1(1) %), and vanadium(V) container (GEM data only), respectively.

their refined weight fractions were 1.1(1) and 4.1(1)%, respectively. The ratio of monoclinic to orthorhombic $Bi_{0.9}La_{0.1}MnO_3$ phases did not change in the 150 or 20 K data. Rietveld profiles are shown in Figure 2, and refinement results are summarized in Table 2. The cell parameters of $Bi_{0.9}La_{0.1}MnO_3$ are slightly smaller than those of $BiMnO_3$ in keeping with the slight difference between $La^{3+}$and Bi^{3+} radii (1.16 and 1.17 Å, respectively for 8-coordination[28]).

Diffraction patterns of the $Bi_{0.8}La_{0.2}MnO_3$ sample were indexed in the orthorhombic space group *Pnma*, as for $LaMnO_3$, with the atomic positions: Bi/La, 4c (x, 1/4, z); Mn, 4b (0, 0, 1/2); O1, 4c (x, 1/4, z); O2, 8d (x, y, z). The 300 K lattice parameters of a = 5.8648(1) Å, b = 7.6128(2) Å, and c = 5.4548(1) Å show an O′-type orthorhombic relationship ($b/\sqrt{2} < c < a$), consistent with orbital order. A secondary monoclinic $Bi_{1-x}La_xMnO_3$ $C2/c$ phase, assumed to have the bulk x = 0.2 composition, and Mn_3O_4 and α-Bi_2O_3 were also observed, with weight fractions of 10.3(3), 2.8(1), and 1.6(1)%, respectively. Rietveld profiles for $Bi_{0.8}La_{0.2}MnO_3$ are shown in Figure 3, and the unit cell parameters, atomic positions, and bond lengths are listed in Table 3. Low temperature diffraction patterns at 20 K showed no splittings or superlattice peaks (except those from the magnetic superstructure described later), indicating the absence of any structural phase transition for the *Pnma* phase.

3.2. Magnetic Structures. The neutron diffraction pattern of $BiMnO_3$ at 20 K did not show any extra peaks when compared to the 150 K diffraction data. However, the intensities of some peaks at low d spacing were increased, showing that ferromagnetic order is present. A ferromagnetic structure was included in the 20 K refinement, with the magnetic components of the two Mn sites constrained to be the same, resulting in a

dx.doi.org/10.1021/cm202900v | *Chem. Mater.* 2012, 24, 199–208

Table 2. Refinement Results for Monoclinic $BiMnO_3$ and $Bi_{0.9}La_{0.1}MnO_3$ at 20 and 150 K (NPD) and 300 K (XRD)[a]

		$BiMnO_3$			$Bi_{0.9}La_{0.1}MnO_3$		
		20 K[b]	150 K[b]	300 K[c]	20 K[b]	150 K[b]	300 K[c]
a (Å)		9.5236(1)	9.5262(2)	9.5386(2)	9.542(2)	9.547(2)	9.5508(3)
b (Å)		5.5996(1)	5.6029(1)	5.6105(1)	5.5846(9)	5.588(1)	5.5913(2)
c (Å)		9.8387(1)	9.8453(2)	9.8570(2)	9.840(2)	9.850(2)	9.8513(3)
β (°)		110.578(1)	110.634(2)	110.640(1)	110.507(2)	110.566(2)	110.615(2)
V (Å^3)		491.20(1)	491.78(1)	493.65(2)	491.1(2)	492.0(3)	492.39(3)
Bi	x	0.1363(1)	0.1362(1)	0.1356(2)	0.1358(2)	0.1340(2)	0.1357(2)
	y	0.2171(2)	0.2184(2)	0.2224(2)	0.2236(2)	0.2248(3)	0.2187(2)
	z	0.1266(1)	0.1266(1)	0.1283(2)	0.1284(2)	0.1264(4)	0.1254(2)
	U_{iso} (Å^2)	0.0008(2)	0.0006(2)	0.0016(2)	0.0038(3)	0.0038	0.0006
Mn	Mn1:y	0.2100(5)	0.2099(6)	0.2213(7)	0.2198(7)	0.300(2)	0.224(1)
	m_y (μ_B)	3.83(2)	–	–	3.73(2)	–	–
	U_{iso} (Å^2)	0.0008(2)	0.0006(2)	0.0019(4)	0.0022(5)	0.0022	0.0006
O1	x	0.0978(2)	0.0982(2)	0.0938(2)	0.0949(3)	0.099(3)	0.090(2)
	y	0.1734(3)	0.1725(4)	0.1816(4)	0.1812(5)	0.187(3)	0.196(4)
	z	0.5807(2)	0.5803(2)	0.5806(2)	0.5810(2)	0.595(2)	0.571(2)
O2	x	0.1462(2)	0.1456(2)	0.1464(2)	0.1465(2)	0.158(3)	0.152(3)
	y	0.5687(2)	0.5702(3)	0.5585(3)	0.5590(3)	0.558(4)	0.552(4)
	z	0.3670(2)	0.3675(2)	0.3661(2)	0.3656(3)	0.386(3)	0.375(3)
O3	x	0.3535(2)	0.3535(2)	0.3552(3)	0.3558(3)	0.369(3)	0.351(3)
	y	0.5463(3)	0.5465(3)	0.5420(4)	0.5434(4)	0.567(4)	0.539(4)
	z	0.1636(2)	0.1641(2)	0.1633(3)	0.1636(3)	0.165(2)	0.162(2)
	U_{iso} (Å^2)	0.0048(2)	0.0043(2)	0.0072(1)	0.0093(3)	0.0093	0.0043
Mn1–O (Å)		2.185(1)	2.193(2)	2.23(2)	2.162(2)	2.167(2)	2.07(2)
		1.916(2)	1.910(3)	1.99(2)	1.911(3)	1.913(3)	1.95(2)
		1.974(3)	1.974(3)	2.02(2)	1.993(4)	1.990(4)	2.07(2)
Mn1–BVS		3.06	3.07	2.60	3.07	3.06	2.90
Mn2–O (Å)		1.930(1)	1.927(2)	1.91(2)	1.956(2)	1.951(2)	2.01(3)
		2.228(1)	2.235(2)	2.11(2)	2.184(2)	2.189(2)	2.17(2)
		1.936(2)	1.939(2)	1.95(2)	1.952(2)	1.951(3)	1.92(2)
Mn2–BVS		3.07	3.06	3.30	3.00	3.01	3.00
R_{wp} (%)		2.25	2.51	3.13	5.68	5.41	4.09
χ^2		1.71	1.43	1.96	5.65	4.95	4.06

[a]Lattice parameters; atomic positions, isotropic thermal factors, and magnetic moments; selected bond distances and BVSs; and R_{wp} and χ^2 residuals are listed. [b]GEM NPD data. [c]D8 XRD data. Atom positions are Bi/La, 8f (x, y, z); Mn1, 4e (0, y, 3/4); Mn2, 4d (1/4,1/4, 1/2); O sites, 8f (x, y, z) in monoclinic spacegroup $C2/c$ (No. 15). R_{wp} values for 150 and 20 K data are total R_{wp} for five histograms (GEM detector banks 1–5) refined simultaneously. The magnetic components m_y for Mn1 and Mn2 at 20 K were constrained to be the same. The isotropic thermal factors of Bi/Mn and oxygen were constrained separately at 20 and 150 K, while the U_{iso} values of 300 K were adopted from 150 K data without refining. Bi/La ratios were held at the nominal values.

refined magnetic moment of 3.77(2) μ_B along the b axis. This is close to the ideal value of 4 μ_B for Mn^{3+} ($3d^4$). The nuclear structure and the magnetic ordering of $BiMnO_3$ are illustrated in Figure 4.

The $Bi_{0.9}La_{0.1}MnO_3$ sample also showed the superposition of the magnetic and nuclear reflections below the magnetic transition temperature (Figure 2b,c). However, an extra peak at d spacing of ~7.6 Å was also observed from this sample at 20 K, which could not be indexed in the $C2/c$ model. This was assigned as a magnetic peak from the antiferromagnetic structure of the orthorhombic $Bi_{1-x}La_xMnO_3$ component and was fitted using the model described below for the x = 0.2 sample, assuming the ordered Mn moments in the two x = 0.1 phases to be equal. The refined magnetic moment of 3.73(2) μ_B is similar to that of $BiMnO_3$. The fit (Figure 2c) is generally good, although the underestimated intensity of the 7.6 Å magnetic peak may reflect a slight normalization error of the long d space data.

The diffraction pattern of $Bi_{0.8}La_{0.2}MnO_3$ at 20 K exhibited a very intense reflection at d spacing of ~7.6 Å and other peaks that were absent from the 150 K NPD pattern (Figure 3b,c). These extra reflections are indexed by the orthorhombic cell but violate the reflection conditions for the *Pnma* space group, indicating that $Bi_{0.8}La_{0.2}MnO_3$ has an antiferromagnetic structure, similar to that of $LaMnO_3$. These additional low temperature peaks are described well by an A-type antiferromagnetic structure in magnetic group *Pnma*,[27] where the spins are ordered ferromagnetically in the *ac* plane and antiferromagnetically along the *b* axis. The nuclear structure and magnetic ordering in $Bi_{0.8}La_{0.2}MnO_3$ are illustrated in Figure 4b. The refined magnetic moment for the Mn^{3+} cation along the *a* axis was 3.89(1) μ_B at 20 K, which is comparable to values reported for $LaMnO_3$ of 3.65(3) μ_B at 14 K[27] or 3.87(3) μ_B at 1.4 K.[38]

dx.doi.org/10.1021/cm202900v | Chem. Mater. 2012, 24, 199–208

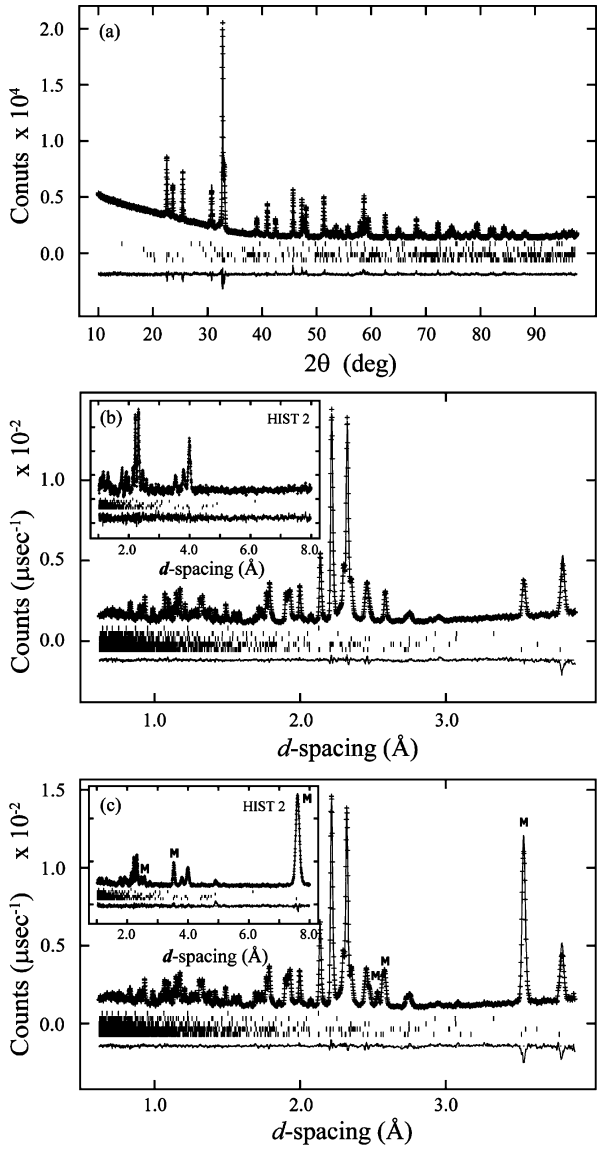

Figure 3. Rietveld fits of $Bi_{0.8}La_{0.2}MnO_3$ for (a) D8 XRD pattern at room temperature, (b) GEM NPD pattern from bank 4 and 2 (inset) at 150 K, and (c) GEM NPD pattern from bank 4 and 2 (inset) at 20 K, while the magnetic reflections are marked by "M". The index markers from the bottom represent the reflections of $Bi_{0.8}La_{0.2}MnO_3$ (85(2) %), Bi/$LaMnO_3$ monoclinic phase (10.3(3) %), Mn_3O_4 (2.8(1) %), α-Bi_2O_3 (1.6(1) %), and V container (GEM data only), respectively.

3.3. Magnetization Measurements. Temperature dependent zero-field-cooled (ZFC) and field-cooled (FC) magnetization measurements in the temperature range 5 to 300 K and at an applied field of 100 Oe are shown in Figure 5. It is evident from the plots that x = 0.0 and x = 0.1 samples show ferromagnetic behavior with a pronounced divergence of ZFC and FC curves around 100 and 90 K, respectively. The observed Curie temperature, T_C, of 101 K for $BiMnO_3$ is comparable to the previously reported values of 99−105 K.[22] La doping has a detrimental effect on ferromagnetic correlations of Mn^{3+} ions, and T_C is lowered to 94 K in $Bi_{0.9}La_{0.1}MnO_3$. The inverse magnetic susceptibility plots above 150 K showed a good fit to the Curie−Weiss law for all three samples, and the parameters are reported in Table 1. A cusp was observed at ~80 K in the ZFC curve of the $Bi_{0.8}La_{0.2}MnO_3$ sample, which is similar to the reported weak ferromagnetic behavior of $LaMnO_3$.[39,40] The noticeable strong divergence between the FC and the ZFC curves below the ordering temperature is consistent with the increase of coercive field with x as noted below.

Magnetization-field hysteresis plots in magnetic fields of −70 to 70 kOe at 5 K are shown in Figure 6, and the derived parameters are shown in Table 1. The $BiMnO_3$ sample shows a saturated magnetic moment of M_s = 3.67 μ_B, close to the ideal value of 4 μ_B for Mn^{3+}, but with very little hysteresis. The saturated moment decreases with increasing x in $Bi_{1-x}La_xMnO_3$ compositions, but both the coercive field (H_c) and the remnant magnetization (M_r) increase. The collapse in M_s between x = 0.1 and x = 0.2 is consistent with the transition from the ferromagnetic $C2/c$ phase to the canted antiferromagnetic (weak ferromagnetic) *Pnma* arrangement. Although a magnetic impurity, Mn_3O_4, is present in the x = 0.2 sample, the proportion is too small to account for the observed saturated moment.

3.4. Electrical Characterization. Dielectric properties of ceramic $Bi_{1-x}La_xMnO_3$ samples with x = 0.1 and 0.2 were measured in terms of the real and imaginary part of the impedance, Z' and Z'', respectively. Complex electric modulus

Table 3. Refinement Results for Orthorhombic *Pnma* $Bi_{0.8}La_{0.2}MnO_3$ at 20 and 150 K (NPD) and 300 K (XRD)[a]

$Bi_{0.8}La_{0.2}MnO_3$		20 K[b]	150 K[b]	300 K[c]
a (Å)		5.8578(4)	5.8618(4)	5.8648(1)
b (Å)		7.5877(5)	7.5977(5)	7.6128(2)
c (Å)		5.4508(4)	5.4466(4)	5.4548(1)
V (Å^3)		242.27(5)	242.57(5)	243.55(1)
Bi/La	x	−0.0656(1)	−0.0657(1)	−0.0668(2)
	z	0.9935(2)	0.9929(1)	0.9952(7)
	U_{iso} (Å^2)	0.0079(2)	0.0078(2)	0.0078
Mn	m_x (μ_B)	3.89(1)	–	–
	U_{iso} (Å^2)	0.0010(2)	0.0017(2)	0.0017
O1	x	0.5253(2)	0.5244(1)	0.518(2)
	z	0.0843(2)	0.0856(2)	0.078(2)
O2	x	0.1838(1)	0.1822(1)	0.198(2)
	y	0.0401(1)	0.0401(1)	0.039(2)
	z	0.7857(1)	0.7861(1)	0.784(2)
	U_{iso} (Å^2)	0.0059(2)	0.0063(1)	0.0063
Mn−O (Å)		1.9574(3)	1.9610(2)	1.953(3)
		1.9177(8)	1.9135(7)	1.96(1)
		2.2107(8)	2.2184(7)	2.15(1)
Mn−BVS		3.07	3.06	3.05
Mn−O1−Mn (deg)		151.45(5)	151.21(5)	154.2(8)
Mn−O2−Mn (deg)		151.35(4)	150.98(3)	154.5(6)
R_{wp} (%)		3.60	2.97	3.74
χ^2		2.61	2.07	3.18

[a]Lattice parameters; atomic positions, isotropic thermal factors, and magnetic moments; selected bond distances and BVSs; and R_{wp} and χ^2 residuals are listed. [b]GEM NPD data. [c]D8 XRD data. Atom positions are Bi/La, 4c (x, 1/4, z); Mn, 4b (0, 0, 1/2); O1, 4c (x, 1/4, z); O2, 8d, (x, y, z) in orthorhombic space group *Pnma* (No. 62). R_{wp} values for 20 and 150 K data are total R_{wp} for five histograms (GEM detector banks 1−5) refined simultaneously. The isotropic thermal factors of Bi/Mn and oxygen were constrained separately at 20 and 150 K, while the U_{iso} values of 300 K were adopted from 150 K data without refining. Bi/La ratios were held at the nominal values.

dx.doi.org/10.1021/cm202900v | *Chem. Mater.* 2012, 24, 199−208

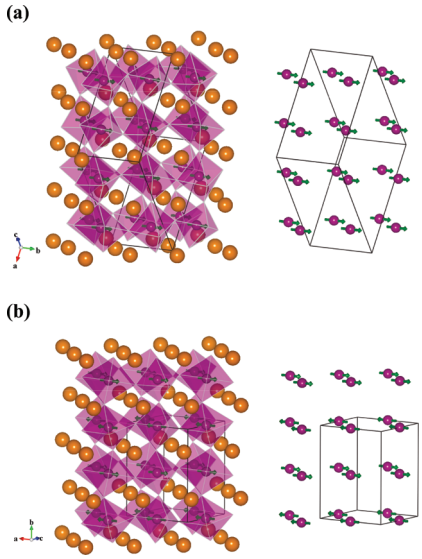

Figure 4. $Bi_{1-x}La_xMnO_3$ crystal and low temperature ordered spin structures for (a), the ferromagnetic $C2/c$ phase (the major component in x = 0 and 0.1 samples), and (b) the antiferromagnetic *Pnma* phase (major component at x = 0.2).

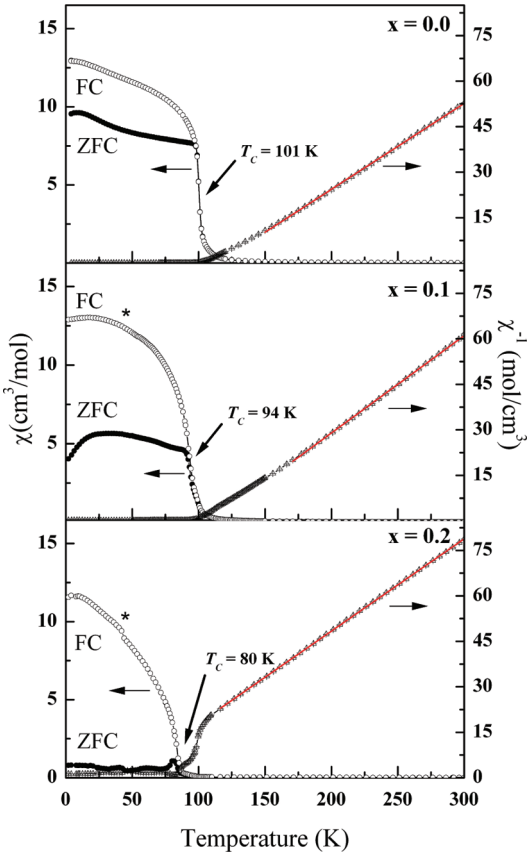

Figure 5. ZFC and FC temperature-dependent magnetization measurements and inverse magnetic susceptibility (ZFC) plots measured from 5 to 300 K in a field of 100 Oe for the $Bi_{1-x}La_xMnO_3$ series. The transition of minor Mn_3O_4 phase is marked by an asterisk.

values were obtained from the impedance using the standard conversion.[41,42] Both x = 0.1 and x = 0.2 samples showed similar impedance responses, and only representative x = 0.1 data are presented here. Data were plotted in the complex plane (as imaginary versus real) for both impedance (Z^*) and modulus

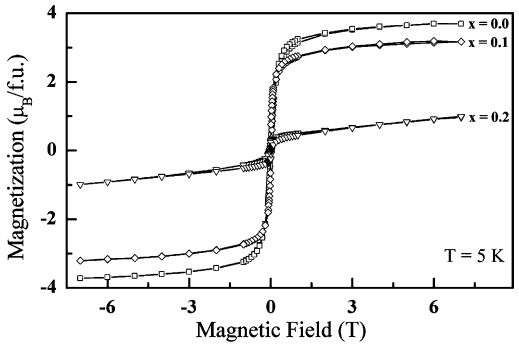

Figure 6. Magnetization-field hysteresis plots for the $Bi_{1-x}La_xMnO_3$ samples at 5 K.

(M^*) formalisms, Figure 7a,b, respectively. The imaginary parts of the impedance, Z'', and the modulus function, M'', as a

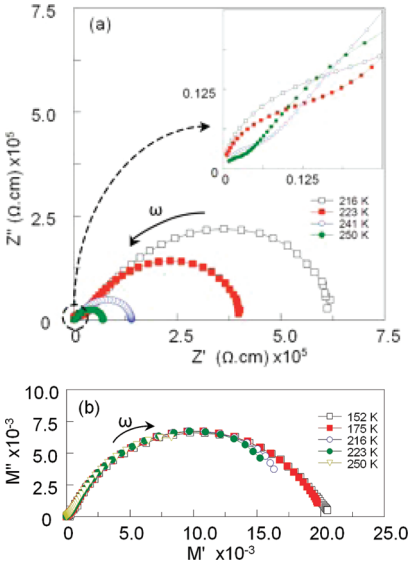

Figure 7. Impedance spectroscopy data: (a) impedance (Z'' vs Z') and (b) electric modulus (M'' vs M') complex plane plots for $Bi_{0.9}La_{0.1}MnO_3$ at temperatures between 150 and 250 K.

function of frequency (f) are shown in Figure 8. The Z'' data show Debye-like peaks with characteristic frequency maxima ($f_{max} = \omega_{max}/2\pi$) as determined by their time constant, $\tau = RC = \omega^{-1}$. Such peaks were not observed at temperatures below about 150 K in the measured range of frequency due to the high total sample resistance. Two poorly resolved semicircles were observed in the Z^* plane plots, suggesting two electroactive regions. Analysis was carried out based on an equivalent circuit based on two parallel RC (resistor and capacitor) elements places in series, consistent with the bricklayer model commonly used for polycrystalline ceramics.[42] At 250 K, the larger, low frequency arc in the Z^* plot has an associated R and C of ca. 65 kΩ·cm and 0.4 nF cm^{-1}, respectively. From the magnitude of the capacitance, this was tentatively attributed to a grain boundary response, although it may also be due to the sample−electrode interface, or chemical inhomogeneity at the sample surface. The high frequency arc (Figure 7a inset) was incomplete at the highest temperatures measured, but below ca. 200 K it was possible to resolve a complete arc both in the complex impedance and the modulus. At 175 K this higher frequency arc has associated R and C of ca. 600 kΩ·cm and

dx.doi.org/10.1021/cm202900v | *Chem. Mater.* 2012, 24, 199−208

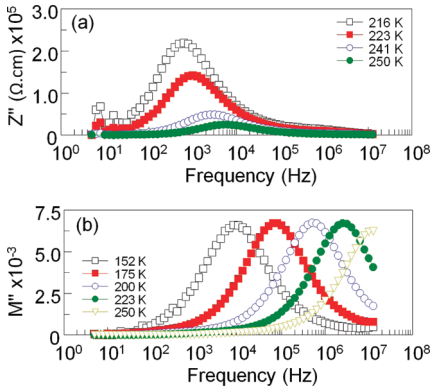

Figure 8. Variation in the (a) imaginary part of impedance (Z'') and (b) imaginary part of modulus function (M'') with frequency for $Bi_{0.9}La_{0.1}MnO_3$ at temperatures 150−250 K.

4 pF cm^{-1} (as estimated from both Z^* and M^* plots). Again the magnitude of the associated C was used to identify the origin of this RC element, here to the bulk response. From the temperature dependence of the Z^*, $Z''(f)$ and $M''(f)$ spectra, Figures 7a and 8a,b, respectively, it can be seen that both the bulk and the grain boundary exhibit an increase in R with decreasing temperature, consistent with a thermally activated conduction process (discussed in more detail below).

Semicircular arcs in M^* scale with inverse relative permittivity (i.e., capacitance), so the data in Figure 7b highlight the bulk response. The M^* data highlight two important points. First, while the arc is incomplete at higher temperatures, it is clear that the (extrapolated) size of the large arc, and therefore bulk relative permittivity, does not show any significant temperature dependence; this is also obvious from the invariant height of the M'' peaks, Figure 8b. Second, the total sample capacitance as determined from the high frequency intercept is completely dominated by the larger arc with very little contribution from the low frequency grain boundary response. To clarify the latter point, for the equivalent circuit used in data analysis the limiting high frequency capacitance, C_{hf}, is given by the expression:[43]

$$C_{hf} = [C_b^{-1} + C_{gb}^{-1}]^{-1}$$

In this case, as $C_{gb} \gg C_b$ the expression simplifies to the approximation that $C_{hf} \approx C_b$. The relative permittivity of the bulk was determined in two ways: from the magnitude of the large arc in M^* plots ($= 1/\varepsilon_r$), and at low temperatures, where it was not possible to distinguish an arc in M^*, from capacitance measured at 1 MHz according to the standard expression $C_p = \varepsilon_r\varepsilon_0 A/d$, where ε_0 is the permittivity of free space and A and d are the electrode area and separation, respectively. Figure 9 shows the variation of the bulk relative permittivity as a function of temperature. The permittivity is only weakly temperature dependent in both $x = 0.1$ and $x = 0.2$ samples, with no signs of anomalies corresponding to the observed crystallographic difference and magnetic ordering transitions. There is good agreement with data obtained from the complex modulus and fixed frequency (obtained both isothermally and during cooling at 2 K min^{-1}). Dielectric loss ($\tan\delta$) data collected at 1 MHz also show no anomalies at the expected transition temperatures; at temperatures > ca. 150 K the dielectric losses increase dramatically due to the increasing sample conductivities. The 20% La sample appears to have a slightly higher relative permittivity ($\varepsilon_r \approx 65$−80) in the

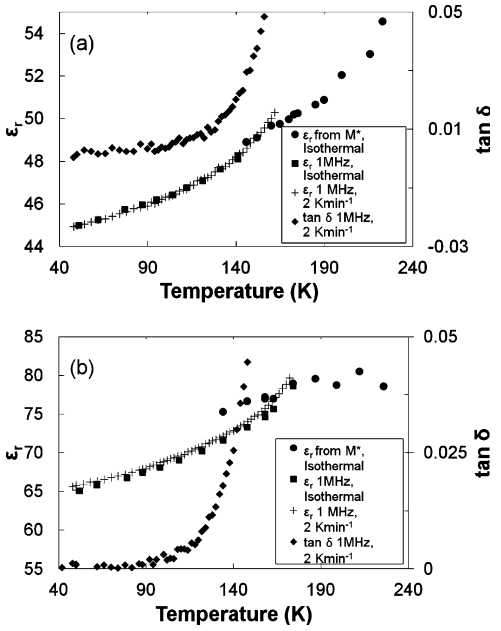

Figure 9. Dielectric data showing relative permittivity and loss for (a) $Bi_{0.9}La_{0.1}MnO_3$ and (b) $Bi_{0.8}La_{0.2}MnO_3$ at temperatures 40−240 K.

temperature range studied compared to the 10% sample ($\varepsilon_r \approx 45$−55). As discussed below this is not attributable to errors associated with measuring sample/electrode geometry or any microstructural variations.

Bulk conductivity data, $\sigma_b = (R_b)^{-1}$, were determined from M^* plots using the expression $R_b = (\omega_{max}C_b)^{-1}$, where $\omega_{max} = 2\pi f_{max}$. The temperature dependence of conductivity is plotted in Arrhenius format in Figure 10a. The linear dependence

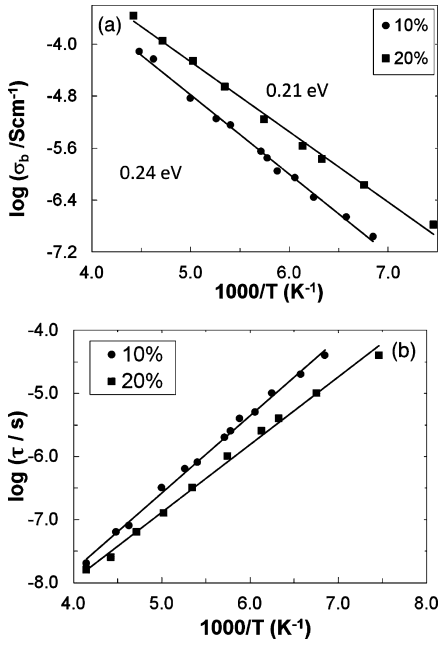

Figure 10. Arrhenius plots of (a) bulk conductivity and (b) bulk time constant for $Bi_{0.9}La_{0.1}MnO_3$ and $Bi_{0.8}La_{0.2}MnO_3$.

clearly shows that the conductivities of both $x = 0.1$ and $x = 0.2$ samples are thermally activated with similar activation energies in the region 0.21−0.24 eV. In order to check that the variation in magnitude of both relative permittivity and conductivity,

dx.doi.org/10.1021/cm202900v | Chem. Mater. 2012, 24, 199−208

time constant data, τ, for each sample, as obtained from f_{max} of M'' peaks, were also plotted in Arrhenius format, Figure 10b. Time constant data have the advantage of being geometry-independent, also remove any systematic error due to fitting of semicircular arcs, and so are useful parameters for comparison. The data show a linear dependence again with similar activation energies (0.24 eV for $x = 0.1$ and 0.21 eV for $x = 0.2$) but with a displacement on the y-axis indicating that the differences in magnitudes of permittivity and conductivity in Figures 9 and 10a are not artificial.

Impedance data were also collected under dc bias, Figure 11. Interestingly the bulk response is unchanged, but the grain

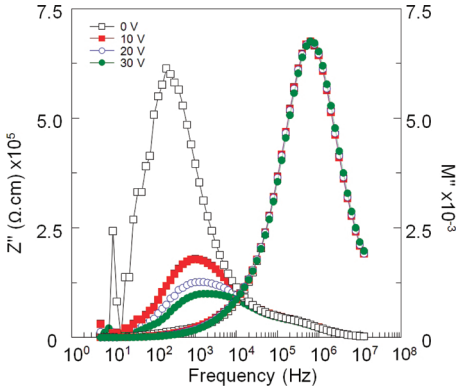

Figure 11. Variations of impedance and electric modulus with applied dc bias for $Bi_{0.9}La_{0.1}MnO_3$.

boundary response shows a large voltage dependence. Such behavior is not expected for simple conduction processes and instead suggests the presence of a Schottky barrier due to a depletion region at the grain boundary. A Mott–Schottky plot (C^{-2} vs field)[44] of the grain boundary capacitance, Figure 12,

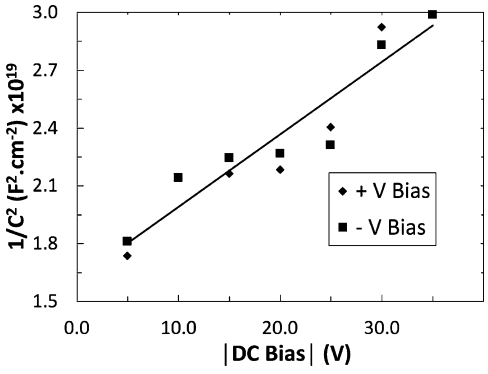

Figure 12. Mott–Schottky plot ($1/C^2$ vs bias voltage) for the grain boundary response of $Bi_{0.9}La_{0.1}MnO_3$.

shows approximate linear behavior and confirms an energy barrier at the grain boundary–bulk junction.

4. DISCUSSION

The above results show that good quality bulk $Bi_{1-x}La_xMnO_3$ solid solutions (>85% phase pure) with low La contents $x \leq 0.2$ can be synthesized at high pressures, where the optimum synthesis pressure decreases from 6 GPa at $x = 0$ to 3 GPa for $x = 0.2$. The phase boundary between the monoclinic $C2/c$ and orthorhombic *Pnma* phases lies between $x = 0.1$ and $x = 0.2$. This transition is first order, and small amounts of the orthorhombic and monoclinic phases are found in the predominantly monoclinic $x = 0.1$ and orthorhombic $x = 0.2$ samples, respectively. From the respective monoclinic:orthorhombic phase ratios of 89.8:5.0 and 10.3:85.3, the linearly interpolated transition composition (at which the ratio becomes 50:50) is $x = 0.153$.

The neutron-refined *Pnma* $Bi_{0.8}La_{0.2}MnO_3$ crystal structure is very similar to that of orbitally ordered $LaMnO_3$,[45] and it is useful to compare the two structures. The *Pnma* unit cell parameters for $LaMnO_3$ are $a = 5.747$, $b = 7.693$, and $c = 5.537$ Å, showing that that the perovskite supercell is slightly less distorted than that of $Bi_{0.8}La_{0.2}MnO_3$ (Table 3). The three distinct octahedral Mn–O distances in $LaMnO_3$ of 1.968, 1.907, and 2.178 Å are very similar to those in $Bi_{0.8}La_{0.2}MnO_3$, demonstrating that the orbital order does not change between $x = 0.2$ and 1.0. However, there is a change in the octahedral tilting, as the Mn–O–Mn angles are 155° in $LaMnO_3$, but are 151° in $Bi_{0.8}La_{0.2}MnO_3$. Hence the increase in lattice distortion on replacing 80% of the La^{3+} in $LaMnO_3$ by Bi^{3+} is due to increased octahedral tilts rather than any change in the orbital ordering (Jahn–Teller distortions) of Mn^{3+}, and we attribute this change to the local lone-pair distortions of Bi^{3+}, as evidenced in other Bi perovskite solid solutions.[46−48] The low temperature neutron fits also confirm that the antiferromagnetic structure of $Bi_{0.8}La_{0.2}MnO_3$ is very similar to that of orbitally ordered $LaMnO_3$.

The reported ferromagnetic properties of $Bi_{0.9}La_{0.1}MnO_3$ thin films were attributed to the presence of Mn^{4+} ions induced by Bi site deficiency.[15] However, all of our bulk $Bi_{1-x}La_xMnO_3$ solid solutions are cation and oxygen stoichiometric by neutron diffraction, and the bond valence sums in Tables 2 and 3 confirm that Mn^{3+} is present throughout. This is corroborated by the paramagnetic moments in Table 1 and the ordered moments observed by neutron diffraction. Ferromagnetism is intrinsic to the monoclinic $C2/c$ $Bi_{1-x}La_xMnO_3$ ($x = 0.0$ and 0.1) phases as confirmed here by magnetization measurements and neutron diffraction. Orthorhombic $Bi_{0.8}La_{0.2}MnO_3$ is an orbitally ordered A-type antiferromagnet, like $LaMnO_3$ in which weak ferromagnetism (canted antiferromagnetism) is observed;[27] however, the presence of ~10% of the monoclinic phase leads to an enhanced ferromagnetic moment in the bulk $x = 0.2$ sample.

Electrical data indicate that both $x = 0.1$ and 0.2 $Bi_{1-x}La_xMnO_3$ ceramics have modest bulk relative permittivites in the range 45–80. The origin of this variation is not clear but may relate in some part to the small difference in unit cell volume. The total polarizability does not scale with the Bi^{3+}:La^{3+}ratio; Bi^{3+} has a higher ionic polarizability than La^{3+} so one would expect higher permittivity in the Bi-rich $x = 0.1$ sample. The presence of point defects associated with a small degree of nonstoichiometry may also play a role, and so the values reported may not be fully intrinsic; electrical behavior is known to be very sensitive to such defects at levels well below those detectable to diffraction and other analytical ones. The dielectric data show no anomalies associated with the structural change or the magnetic ordering transitions.

In both $x = 0.1$ and 0.2 bulk ceramics, the bulk conductivity is sufficient to preclude testing for ferroelectric hysteresis even at room temperature. The conduction process is thermally activated in both compounds with activation energies of the order of 0.21–0.24 eV. From the magnitude of these values, the condution is likely to be dominated by an electronic rather than an ionic process, although it is not clear whether this

dx.doi.org/10.1021/cm202900v | *Chem. Mater.* 2012, 24, 199–208

conductivity is n- or p-type. Transition metal oxide ceramics are well-known to accommodate oxygen nonstoichiometry leading to mixed valency and electronic point defects which dominate conduction processes.[49] The Mott−Schottky behavior observed under dc bias strongly suggests the presence of depletion layers and n-p-n (or p-n-p) junctions at the bulk−grain boundary interfaces, and this may provide an additional clue as to the origins of electrical behavior. Kalantari et al.[50] recently reported an activation energy of 0.29 eV for bulk conductivity in the related material $Bi_{0.85}Nd_{0.15}FeO_3$ and attributed it to a polaronic hopping mechanism due to oxygen loss and subsequent mixed $Fe^{3+/2+}$ valency. It is likely in our samples that the bulk is similarly oxygen deficient:

$$O_O^X \rightarrow \frac{1}{2}O_{2(g)} + 2e'$$

resulting in partial reduction of Mn^{3+} to Mn^{2+} and a similar polaronic (n-type) mechanism. Partial reoxidation at the grain boundaries on cooling would create a depletion layer.[51−53] In addition the grain surfaces may be Bi deficient, compensated by oxygen vacancies in a partial Schottky defect reaction:

$$2Bi_{Bi}^X + 3O_O^X \Rightarrow 2V_{Bi}''' + 3V_O^{\cdot\cdot} + \uparrow 2Bi_{(vap)} + \frac{3}{2}O_{2(g)}$$

Again, on cooling the grain boundaries are partially reoxidized generating holes and a p-type (acceptor) regime:

$$\frac{1}{2}O_{2(g)} + V_O^{\cdot\cdot} \Rightarrow O_O^X + 2h^{\cdot}$$

As the defect reaction for each mechanism has a specific stoichiometric relationship between carrier concentration and oxygen partial pressure pO_2, the variation of conductivity with changes in pO_2 is typically used to corroborate the mechanism and determine whether the conduction is n- or p-type. Such measurements cannot be conducted here as the temperatures at which it is possible to observe the bulk conductivity are in the regime where the kinetics of oxygen diffusion would be impossibly slow. Annealing at high temperatures in varying pO_2 followed by conductivity measurements is not possible due to the metastability of the compounds at ambient pressure. Thermopower measurements may allow identification of n- or p-type behavior in a future study.

5. CONCLUSIONS

La-substituted $BiMnO_3$ perovskite oxides have been prepared under high pressure and characterized by X-ray and neutron diffraction and magnetic electrical measurements. The perovskite superstructure changes from monoclinic $C2/c$ to orthorhombic $Pnma$ at $x = 0.15$ for samples prepared at 3−4 GPa. The $C2/c$ phase is ferromagnetic throughout, but La substitution depresses T_C from 101 K in $BiMnO_3$ to 94 K in $Bi_{0.9}La_{0.1}MnO_3$. The $Pnma$ phase $Bi_{0.8}La_{0.2}MnO_3$ shows a very similar crystal structure, including Mn^{3+} orbital ordering and A-type antiferromagnetism to $LaMnO_3$. These bulk $Bi_{1-x}La_xMnO_3$ samples prepared at high pressure appear stoichiometric by neutron diffraction and magnetic measurments, but a residual conductivity suggests that a low level of electronic carriers are present. Impedance spectroscopy measurements do not suggest any ferroelectric behavior in $x = 0.1$ and $x = 0.2$ samples, and modest values of dielectric constant were observed. Different behavior reported for thin films may reflect strain, off-stochiometry, or electrode effects. Activation energies in the range of 0.21−0.24 eV were calculated from the thermally activated Arrhenius fit on conductivity data.

■ ACKNOWLEDGMENTS

We thank EPSRC, STFC, Leverhulme Trust, Royal Society of Edinburgh, and Royal Society, UK, and Lahore University of Management Sciences and Higher Education Commission, Pakistan, for support.

■ REFERENCES

(1) Eerenstein, W.; Mathur, N. D.; Scott, J. F. *Nature* **2006**, *442*, 759.
(2) Ramesh, R.; Spaldin, N. A. *Nat. Mater.* **2007**, *6*, 21.
(3) Baettig, P.; Seshadri, R.; Spaldin, N. A. *J. Am. Chem. Soc.* **2007**, *129*, 9854.
(4) Claridge, J. B.; Hughes, H.; Bridges, C. A.; Allix, M.; Suchomel, M. R.; Niu, H.; Kuang, X.; Rosseinsky, M. J.; Bellido, N.; Grebille, D.; Perez, O.; Simon, C.; Pelloquin, D.; Blundell, S. J.; Lancaster, T.; Baker, P. J.; Pratt, F. L.; Halasyamani, P. S. *J. Am. Chem. Soc.* **2009**, *131*, 14000.
(5) Selbach, S. M.; Tybell, T.; Einarsrud, M. A.; Grande, T. *Chem. Mater.* **2009**, *21*, 5176.
(6) Belik, A. A.; Kolodiazhnyi, T.; Kosuda, K.; Muromachi, E. T. *J. Mater. Chem.* **2009**, *19*, 1593.
(7) Schmid, H. *Ferroelectrics* **1994**, *162*, 665.
(8) Gajek, M.; Bibes, M.; Fusil, S.; Bouzehouane, K.; Fontcuberta, J.; Barthelemy, A.; Fert, A. *Nat. Mater.* **2007**, *6*, 296.
(9) Jiang, Q. H.; Nan, C. W.; Shen, Z. J. *J. Am. Chem. Soc.* **2006**, *89*, 2123.
(10) Catalan, G.; Scott, J. F. *Adv. Mater.* **2009**, *21*, 2463.
(11) Martin, L. W. *Dalton Trans.* **2010**, *39*, 10813.
(12) van Aken, B. B.; Palstra, T. T. M.; Filippetti, A.; Spaldin, N. A. *Nat. Mater.* **2004**, *3*, 164.
(13) Kimura, T.; Goto, T.; Shintani, H.; Ishizaka, K.; Arima, T.; Tokura, Y. *Nature* **2003**, *426*, 55.
(14) Hur, N.; Park, S.; Sharma, P. A.; Ahn, J. S.; Guha, S.; Cheong, S.-W. *Nature* **2004**, *429*, 392.
(15) Gajek, M.; Bibes, M.; Wyczisk, F.; Varela, M.; Fontcuberta, J.; Barthelemy, A. *Phys. Rev. B* **2007**, *75*, 174417.
(16) Sugawara, F.; Iida, S.; Syono, Y.; Akimoto, A. *J. Phys. Soc. Jpn.* **1968**, *25*, 1553.
(17) Khomskii, D. I. *J. Magn. Magn. Mater.* **2006**, *306*, 1.
(18) dos Santos, A. M.; Parashar, S.; Raju, A. R.; Zhao, Y. S.; Cheetham, A. K.; Rao, C. N. R. *Solid State Commun.* **2002**, *122*, 49.
(19) Sharan, A.; Lettieri, J.; Jia, Y.; Tian, W.; Pan, X.; Schlom, D. G.; Gopalan, V. *Phys. Rev. B* **2004**, *69*, 214109.
(20) Chiba, H.; Atou, T.; Syono, Y. *J. Solid State Chem.* **1997**, *132*, 139.
(21) Baetting, P.; Seshardi, R.; Spaldin, N. *J. Am. Chem. Soc.* **2007**, *129*, 129.
(22) Belik, A. A.; Iikubo, S.; Yokosawa, T.; Kodama, K.; Igawa, N.; Shamoto, S.; Azuma, M.; Takano, M.; Kimoto, K.; Matsui, Y.; Takayama-Muromachi, E. *J. Am. Chem. Soc.* **2007**, *129*, 971.
(23) Kimura, T.; Kawamoto, S.; Yamada, I.; Azuma, M.; Takano, M.; Tokura, Y. *Phys. Rev. B* **2003**, *67*, 180401.
(24) Belik, A. A.; Yusa, H.; Hirao, N.; Ohishi, Y.; Takayama-Muromachi, E. *Inorg. Chem.* **2009**, *48*, 1000.
(25) Kozlenko, D. P.; Belik, A. A.; Kichanov, S. E.; Mirebeau, I.; Sheptyakov, D. V.; Strässle, Th.; Makarova, O. L.; Belushkin, A. V.; Savenko, B. N.; Takayama-Muromachi, E. *Phys. Rev. B* **2010**, *82*, 014401.
(26) Belik, A. A.; Kodama, K.; Igawa, N.; Shamoto, S.; Kosuda, K; Takayama-Muromachi, E. *J. Am. Chem. Soc.* **2010**, *132*, 8137.
(27) Huang, Q; Santoro, A.; Lynn, J. W.; Erwin, R. W.; Borchers, J. A.; Peng, J. L.; Greene, R. L. *Phys. Rev. B* **1997**, *55*, 14987.
(28) Shannon, R. *Acta Crystallogr., Sect. A* **1976**, *32*, 751.
(29) Seshadri, R.; Hill, N. A. *Chem. Mater.* **2001**, *13*, 2892.
(30) Moreira dos Santos, A. F.; Cheetham, A. K.; Atou, T.; Syono, Y.; Yamaguchi, Y.; Ohoyama, K.; Chiba, H.; Rao, C. N. R. *Phys. Rev. B* **2002**, *66*, 064425.

(31) Troyanchuk, I. O.; Mantytskaja, O. S.; Szymczak, H.; Shvedun, M. Y. *Low Temp. Phys.* **2002**, *28*, 569.
(32) Williams, A. J.; Gillies, A.; Attfield, J. P.; Heymann, G.; Huppertz, H.; Martínez-Lope, M. J.; Alonso, J. A. *Phys. Rev. B* **2006**, *73*, 104409.
(33) Ortega-San-Martin, L.; Williams, A. J.; Rodgers, J.; Attfield, J. P. *Phys. Rev. Lett.* **2007**, *99*, 255701.
(34) Kimber, S. A. J.; Rodgers, J. A.; Wu, H.; Murray, C. A.; Argyriou, D. N.; Fitch, A. N.; Khomskii, D. I.; Attfield, J. P. *Phys. Rev. Lett.* **2009**, *102*, 046409.
(35) Larson, A. C.; von Dreele, R. B. *GSAS-Generalized Crystal Structure Analysis System*; Report No. LA-UR-86-748; Los Alamos National Laboratory: Los Alamos, NM, 1987.
(36) Scribner Associates Inc. *ZView*; Southern Pines, NC, USA, 2000.
(37) Montanari, E.; Calestani, G.; Righi, L.; Gilioli, E.; Bolzoni, F.; Knight, K. S.; Radaelli, P. G. *Phys. Rev. B* **2007**, *75*, 220101(R).
(38) Moussa, F.; Hennion, M.; Rodriguez-Carvajal, J.; Moudden, H.; Pinsard, L.; Revcolevschi, A. *Phys. Rev. B* **1996**, *54*, 15149.
(39) Khomchenko, V.; Troyanchuk, I.; Mantytskaya.; Tovar, O. M.; Szymczak, H. *J. Exp. Theor. Phys.* **2006**, *103*, 54.
(40) Skumryev, V.; Ott, F.; Coey, J. M. D.; Anane, A.; Renard, J. P.; Pinsard-Gaudart, L.; Revcolevschi, A. *Eur. Phys. J. B* **1999**, *11*, 401.
(41) MacDonald, J. R. *Impedance Spectroscopy: Emphasizing Solid State Materials and Systems*; Wiley: New York, 1987.
(42) Irvine, J. T. S.; Sinclair, D. C.; West, A. R. *Adv. Mater.* **1990**, *2*, 132.
(43) Morrison, F. D.; Sinclair, D. C.; West, A. R. *Appl. Phys.* **1999**, *86*, 6355.
(44) Orazem, M. E.;Tribollet, B. *Electrochemical Impedance Spectroscopy*; John Wiley and Sons: New York, 2008.
(45) Rodriguez-Carvajal, J.; Hennion, M.; Moussa, F.; Moudden, A. H.; Pinsard, L; Revcolevschi, A. *Phys. Rev. B* **1998**, *57*, R3189.
(46) Goff, R. J.; Attfield, J. P. *J. Solid State Chem.* **2006**, *179*, 1369.
(47) Chen, W .T.; Williams, A. J.; Ortega-San-Martin, L.; Ming, L.; Sinclair, D. C.; Zhou, W.; Attfield, J. P. *Chem. Mater.* **2009**, *21*, 2085.
(48) Ortega-San-Martin, L.; Williams, A. J.; Storer, A; Attfield, J. P. *Chem. Mater.* **2009**, *21*, 2436.
(49) Smyth, D. M. *The Defect Chemistry of Metal Oxides*,; Oxford University Press: Oxford, 2000.
(50) Kalantari, K.; Sterianou, I.; Karimi, S.; Ferrarelli, M. C.; Miao, S.; Sinclair, D. C.; Reaney, I. M. *Adv.Funct. Mater.* **2011**, *21*, 3737.
(51) Denk, I.; Knoll, F.; Maier, J. *J. Am. Ceram. Soc.* **1997**, *80*, 279.
(52) Lupetin, P.; Gregori, G.; Maier, J. *Angew. Chem., Int. Ed.* **2010**, *49*, 1.
(53) Frömling, T.; Hou, J.; Preis, W.; Sitte, W.; Hutter, H.; Fleig, J. *J. Appl. Phys.* **2011**, *110*, 043531.